

Image processing system for velocity measurements in natural convection flows

S. Ushijima, H. Takeda and N. Tanaka

Central Research Institute of Electric Power Industry (CRIEPI), 1646 Abiko, Abiko-shi, Chiba-ken, 270-11, Japan

Received 1 July 1990

An image processing system based on a particle-tracking method has been developed to measure quantitatively at one time the two-dimensional velocity components arising in natural convection flows. The analysis of the image data proceeds automatically, due in part to the video recording system utilized in our method. The image processing system was applied to the natural convection flows in a 1/10 scale basic reactor model. The velocity vectors and the vorticities were obtained under transient and steady states in different experimental cases, enabling us to examine in detail the transition of the flow patterns and other aspects under different experimental conditions. The uncertainty of this system was evaluated for use in our experiments and it was confirmed that the margin of error is acceptable.

1. Introduction

A decay heat removal system (DHRS) in a fast breeder reactor (FBR), based on the natural convection flow driven only by interior buoyancy forces, is expected to be an effective way to remove the decay heat at the core in the event of the total loss of the electric power supply. The thermal hydraulics aspect of the naturally convected coolant is, in particular, one of the most essential engineering subjects, since it determines the efficiency of the DHRS and it is closely related to the possible thermal damage imposed on internal structures when any deflected flow patterns arise.

Extensive thermal hydraulics studies have been made in an attempt to clarify the behavior of the natural convection flows with reduced-scale models using water as a simulant fluid [1–4]. However, few experimental investigations were conducted to measure the quantitative flow patterns, which are generally characterized by low-Reynolds-number turbulent flows accompanied by different scale eddies changing with time and space.

The purpose of this study is to develop an image processing method, which has already been used in various investigations on fluid dynamics [5], for the specific application of measuring velocity and vorticity arising in a natural convection flow at one time over a two-dimensional plane. The principle of our image

analyses is based on particle-tracking [6], a simple and effective technique that has often been employed to determine flow patterns and velocity since Prandtl and Tietjens [7] and others. Another merit associated with particle-tracking is that the sources and the extent of its uncertainties have already been estimated and clarified [8–12]. Recent advancements in digital processors allowed the use of digital computers in the image analyses. The procedure to digitize photographically recorded images necessary for computer analyses was done manually in early systems [8,13], while automatic digitization has been employed in more recent studies [10].

Taking account of recent advancements in image analyses, this study has emphasized the use of automatic digitization, interpolation and smoothing techniques, and estimation of measurement uncertainties. In our method, visualized movements of small particles in a fluid are recorded on video tapes and then converted to digital data automatically by an image processor. The all numerical analyses of the digital data, such as the determination of velocity vectors and their interpolation, are performed on a computer. The image processing system developed was applied to the natural convection flows in a 1/10 scale reactor model and several distributions of velocity vectors and vorticities were obtained quantitatively during transient periods and steady states. As a result it became possible to examine the detailed behavior of the flows under dif-

ferent experimental conditions. The uncertainties involved in our method were estimated and it was confirmed that the error ranges are acceptable.

2. Experimental procedure

2.1. Natural convection flow experiments

Experiments on the natural convection flows in an FBR have been conducted to understand the basic phenomena occurring in its hot plenum region. The rectangular tank illustrated in fig. 1 is a 1/10 scale model of a primary system in an FBR. It consists of a core, a reflector, hot and cold plena, an above core structure (ACS) and an intermediate heat exchanger (IHx) including a DHRS. The core region consists of an electric heater, whose maximum output is around 2.7 kW, and an acrylic flow-regulator set up above it. The thermal output of the heater can be varied arbitrarily by regulating its input voltage. This heater has thirty holes, each with a diameter of 10 mm, so that the heated fluid can rise up through the core region. In the reflection region, located next to the core, flow resis-

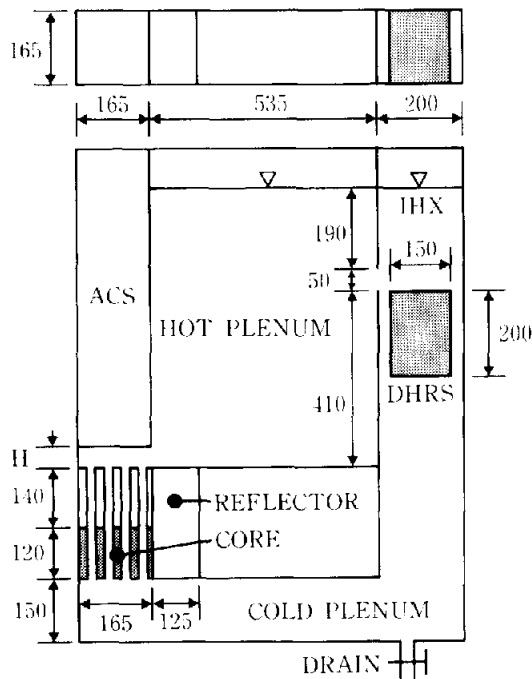


Fig. 1. 1/10 scale experimental model for a primary system in an FBR.

Table 1
Experimental conditions

Case No.	P_0 (kW)	T_s (K)	Q_s (m ³ /s)	T_0 (K)	H (mm)
Case-A35	2.0	278	3.3×10^{-4}	303	35
Case-A50	2.0	278	3.3×10^{-4}	303	50
Case-B35	2.0	278	3.3×10^{-4}	298	35

tance is controlled by attaching a suitable punched plate to its bottom surface. However, in the case presented here, the flow was not permitted through this region. The DHRS is simulated by a water-cooled heat sink installed in the interior of the IHx as indicated in fig. 1. This type of DHRS is usually called PRACS (Primary Reactor Auxiliary Cooling System). The thermal capacity removed by the cooler can be adjusted by the flow rate and the temperature of its secondary flow, and its maximum cooling power is almost equivalent to that of the heater. The total flow rate in the tank depends on the balance between the buoyancy force, created by the heater and the cooler, and the flow resistance incurred by a single circulation pass (core-hot plenum-IHx-cold plenum-core).

The three cases of experiments presented in this paper follow the conditions listed in table 1. In table 1, P_0 is the output of the heater, T_s and Q_s are the temperature and the flow rate of the secondary loop providing the cooler with cooling-water, T_0 means the initial temperature in the hot plenum and H stands for the height of the above core structure (ACS) from the bottom surface of the plenum.

The characteristic quantities, associated with the flow formed in the plenum under steady state conditions, are derived as indicated in table 2. The representative velocity U_0 was evaluated by our image processing method in the vicinity of the IHx window and obtained as an average velocity at the core region using its area (0.165×0.165 m). In addition, the characteristic time t_0 was calculated from the flow rate based on U_0 and the volume of the hot plenum ($0.65 \times 0.535 \times 0.165$ m). The macro-length scale L_0 is the average

Table 2
Characteristic quantities under steady state conditions

Case No.	U_0 (mm/s)	t_0 (s)	L_0 (m)	ΔT (K)
Case-A35	7.98	265	0.593	4.7
Case-A50	5.52	383	0.593	4.6
Case-B35	9.73	217	0.593	5.0

value between the plenum length (0.65 m) and its width (0.535 m). The representative temperature ΔT is the difference between those at the core outlet and the inlet, which corresponds to the maximum temperature difference arising in the experimental tank.

As a nondimensional parameter governing the bulk circulation flow in the experimental tank, one may take up the Richardson number (Ri), which is associated with the balance between the driving force due to the buoyancy and the flow resistance along the pass. In addition, the mixing process of momentum and heat in the hot plenum are closely related to the Reynolds number (Re) and the Péclet number (Pe). The Péclet number becomes important especially when considering the similarity rule between the present water experiments and actual phenomena in an FBR, in which liquid sodium is employed as a coolant. These parameters can be defined as

$$Ri = \frac{\beta g \Delta T L_0}{U_0^2}, \quad (1)$$

$$Re = \frac{U_0 L_0}{\nu}, \quad (2)$$

$$Pe = \frac{U_0 L_0}{\alpha}, \quad (3)$$

where β , g , ν and α are the thermal expansion coefficient, gravity, kinematic viscosity and molecular thermal diffusivity, respectively. The above stated parameters are derived with the values listed in table 2 and they are shown in table 3 together with the estimated numbers for an FBR. As indicated in table 3, the similarity rule based on the Richardson number is reasonably satisfied, since the Richardson numbers in experiments and in an actual reactor are roughly of the same order. While the Reynolds numbers in experiments are lower than the reactor's value by nearly two orders, it is conceivable that a sufficiently turbulent state is attained in our experiments. The reactor's Péclet number, however, is lower than the experimental values, since the liquid sodium has a higher thermal

diffusivity than that of water. Thus it might be necessary to take account of this difference in interpreting the experimental results as the phenomena occurring in an FBR.

2.2. Flow visualization and digitization of image data

Flow-visualization experiments were carried out mainly in the hot plenum of the experimental tank. A suitable quantity of particles were scattered in the tank as tracers for our particle-tracking method. The particles are made of high polymer Eslon, with a specific gravity of 1.03. The shape of the particles is spherical and their diameter is around 0.4 mm. They include fluorescent sodium which gives clear images in the presence of laser light. Saline water was used as a working fluid with a suitable concentration to give the particles neutral buoyancy.

A sheet of laser light was applied as the illumination to visualize a vertical cross-section. The sheet of laser light emitted by argon ions with a maximum power of 5 W was injected from the top of the hot plenum, where the water surface was sufficiently static, and intensified by a plane mirror installed on the bottom surface. The width of the sheet was approximately 5 mm.

The visualized particles were recorded on video tapes with a high-sensitive video camera (Hamamatsu Model C1000) equipped with a front lens which can correct the distortion of the images. The application of video cameras to the particle-tracking method [14] has recently eliminated the need for extensive manual work to analyze photographically recorded images aided by digitizing tablets [8]. The adoption of a video recording system makes it possible to prevent manual-positioning errors and to digitize the image data automatically, which decreases the processing time and increases the amount of analyzable data. The main disadvantages of video recording, on the other hand, probably lie in the spatial resolution and the time interval between video frames, which is usually 1/30 second unless employing a high-speed recording system as briefly mentioned by Racca and Dewey [15]. Nevertheless, the spatial resolution, 512×512 pixels in our method, is not necessarily inferior to most recording systems employing TV or CCD cameras, as by Nishino et al. (490×384 pixels) [9], Chen et al. (340×340 pixels) [16] and Kobayashi et al. (512×480 pixels) [10]. Our recording system produced satisfactory resolution in terms of the uncertainty associated with the visualization error, which is given in detail later. In addition, the time interval of

Table 3
Non-dimensional parameters

Case No.	Ri	Re	Pe
Case-A35	1.2×10^2	5.9×10^3	3.2×10^4
Case-A50	2.5×10^2	4.1×10^3	2.2×10^4
Case-B35	8.9×10^1	7.2×10^3	3.9×10^4
FBR	4.2×10^2	7.8×10^5	4.3×10^3

the frames, 1/30 second, is sufficiently short compared with the interval to obtain the particle trajectories, which are dependent on local velocities.

Our image processing system consists of several sequential procedures as presented in fig. 2. The particle images recorded on video tapes were converted to digital data which can be dealt with by a computer. Our digitized data, which consist of 512×512 pixels with 256-gray-level resolution per single pixel, were obtained from one frame through an image processor

(PIAS LA500) controlled by a personal computer (NEC PC9801VX). The digitized data were stored on hard disks and then transported to magnet tapes, which can be read by a high-speed computer (HITAC M680H), so that the processing time can be minimized. The devices associated with data transfer are shown in fig. 3. The transfer, conducted with a GPIB interface, simultaneously converted the format of the data from ASCII code to hexadecimal form, which stores the data at a rate of two bytes per pixel.

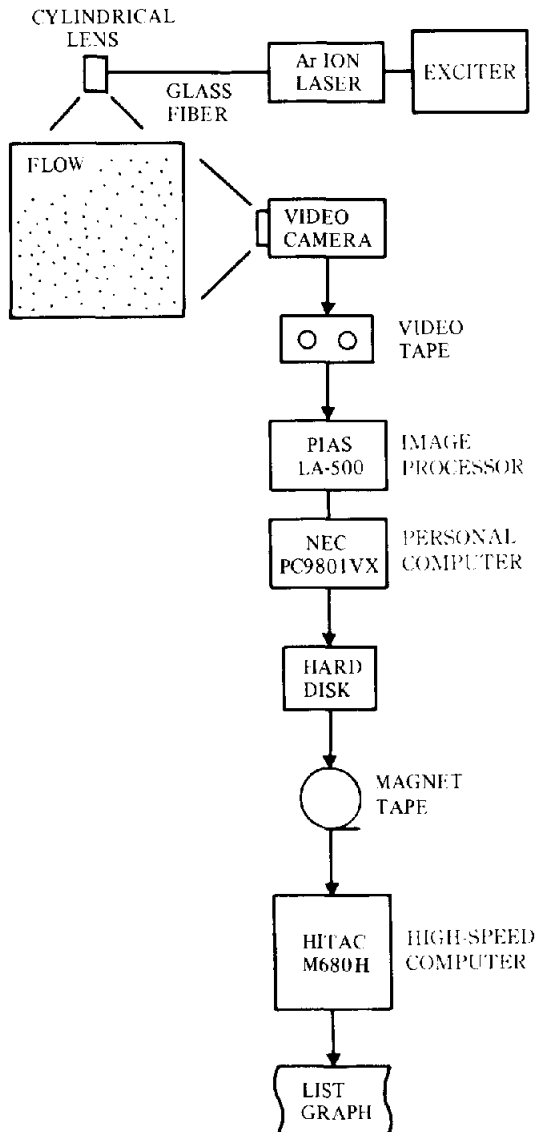


Fig. 2. Sequential procedures for image analyses.

3. Image processing

3.1. Determination of velocity vectors

The velocity vectors of natural convection flows were determined by computer analyses of the transferred image data. The principle of the vector acquisition was essentially equivalent to the method presented by Kobayashi et al. [10], in which both the initial and the terminal positions of the particle in question were used together with its trace image to determine the direction of the vector. Thus, as schematically shown in fig. 4, three kinds of images are necessary to determine one vector: a particle image recorded at $t = t_1$ indicating the initial position, another particle image at $t = t_1 + \Delta t$ corresponding to the terminal position, and a trace image obtained during the time interval Δt . The trace image was created by superimposing four frames on the image processor prior to the data transfer. The time interval Δt was 0.1 second and that of the four frames was equal to $\frac{1}{3}\Delta t$. In the first stage of this vector determination, the three image data were binarized on the basis of a single threshold level, which is considered appropriate by Chang et al. [11]. Then, from the binarized particle images indicating initial and terminal positions, their center points were calculated. The center points were compared with each trace image and were judged valid only when one initial center point and one terminal center point were simultaneously included in a single trace. When the actual distance between the two valid center points is denoted by Δl , the velocity vector at $t = t_1 + 0.5\Delta t$ was finally determined as that having an absolute value of $\Delta l/\Delta t$ and a direction from the initial center point to the terminal one. A few invalid vectors at particle positions P_m , occurring in spite of the above process, are identified by examining whether or not they lie outside the error band, $\mu_{km} \pm 3\sigma_{km}$, where μ_{km} and σ_{km} are mean values and standard deviations, respectively, for the velocity components u_{km} at P_m . The

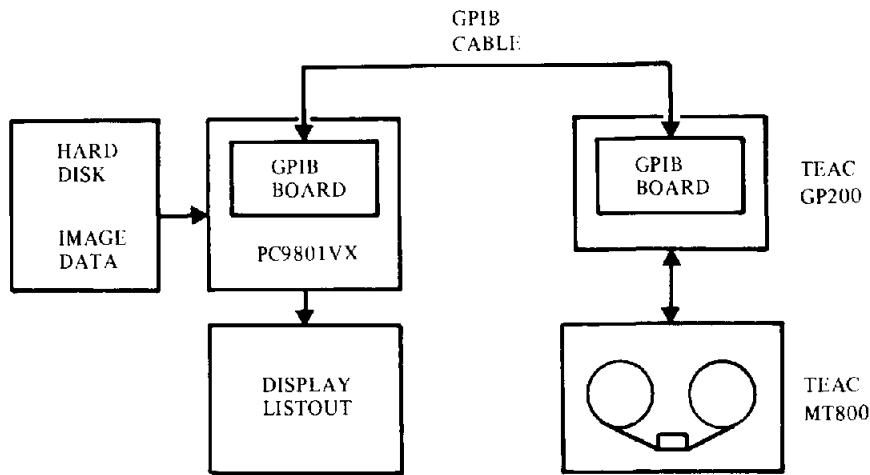


Fig. 3. Relationship of devices associated with data transfer.

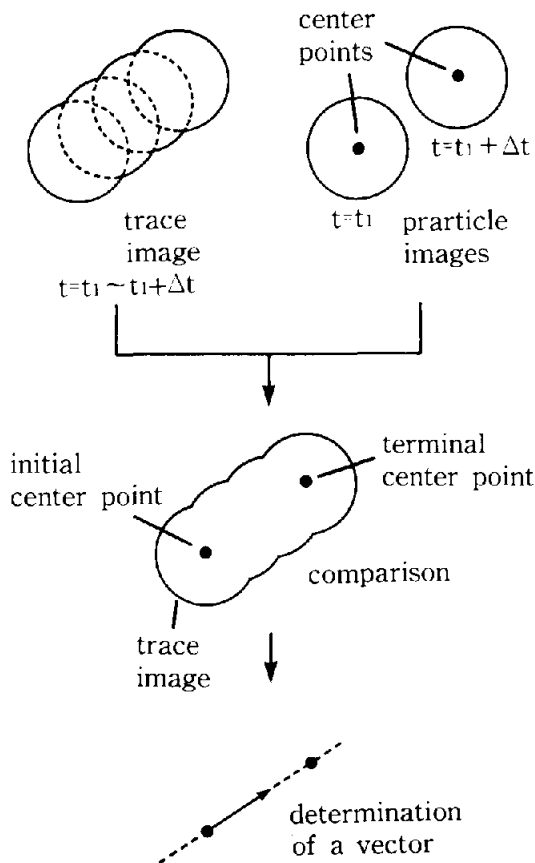


Fig. 4. The principle of vector acquisition.

statistical values u_{km} and σ_{km} are derived from a bootstrap procedure as described in detail later. The vectors judged invalid are replaced by the mean values at P_m .

The velocity vectors at the regular grid points were obtained by interpolating the vectors randomly distributed in accordance with the original particle positions. While various interpolation methods were employed in previous works, Agui and Jimenez [12] concluded that the following Gaussian window is most advantageous compared with polynomial interpolation, kriging, convolutions and others:

$$u_{kij} = \frac{\sum_m \alpha_m u_{km}}{\sum_m \alpha_m}, \quad (4)$$

where u_{kij} is the velocity component at the grid point P_{ij} and u_{km} indicates the known velocity component at the particle positions P_m . The subscript k defines the component ($k = 1$ or 2); for instance, u_{1m} and u_{2m} are the horizontal and vertical velocity components at P_m , respectively. Using the coordinates (x_{1ij}, x_{2ij}) and (x_{1m}, x_{2m}) for P_{ij} and P_m , respectively, the weighting coefficient α_m is given by

$$\alpha_m = \exp \left[\frac{- \left\{ \sum_k (x_{km} - x_{kij})^2 \right\}}{H_w^2} \right]. \quad (5)$$

The optimum window width H_w proposed by Agui and

Jimenez is 1.24δ , where δ is the mean distance between particles. The distance δ is calculated by

$$\delta = (1/\pi N)^{1/2}, \quad (6)$$

where N is the average number of particles per unit surface. The number N was counted as that of the particles providing valid trace images in each frame and the window width $H_w = 1.24 \delta$ was applied to our interpolation procedure based on the eqs. (4) and (5). While the values of N and δ are different in accordance with the flow aspects, their mean values were $9.8 \times 10^{-3} \text{ mm}^{-2}$ and 5.9 mm , respectively, in our experiments. In terms of the Nyquist sampling criterion, the resolution for the highest wavenumber is limited by $1/(2\delta)$ [12], which indicates that meaningful mesh intervals, Δx , and Δx_z , should be larger than 2.6. Taking account of this fact, a uniform grid ($\Delta x = \Delta x_z$) was set up with its interval, 13 mm , slightly larger than 2.6.

The appearance of some errors cannot be prevented during the interpolation process. Agui and Jimenez [12] conducted numerical experiments and evaluated the interpolation error arising in a synthetic velocity field by means of a bootstrap procedure [17,18]. The bootstrap allows us to draw a frequency distribution for the possible velocities at the grid point and as a result the error range, such as a standard deviation, can be estimated for each interpolated result. Agui and Jimenez proposed a smoothing technique, in which the interpolated velocity is filtered as smoothly as possible in the space within the error 'layer' determined by the error ranges at all grid points. Our velocity fields were also spatially averaged by solving the Laplace equation, $\nabla^2 u_{kij} = 0$, with the aid of this concept. The averaged velocity component $u_{ave,kij}^{n+1}$, which is the solution of the successive relaxation method at step $n+1$, was derived with four immediate neighbors at step n as

$$u_{ave,kij}^{n+1} = \frac{1}{4} (u_{ki-1j}^n + u_{ki+1j}^n + u_{kij-1}^n + u_{kij+1}^n). \quad (7)$$

The error range at the corresponding grid point was, on the other hand, determined from the originally interpolated velocity components u_{kij} with the following bootstrap procedure:

(1) A base sample is formed from all original velocity components u_{kij} whose total number is N .

(2) A synthetic sample is created by selecting vectors randomly from the base sample. Since the number of the selected components equals that of the base sample (N), some of the original components are possibly chosen more than one time while others would not be present at all.

(3) Many of the synthetic samples, with the number n_1 , are generated in the same way.

(4) New velocity components are obtained at the grid points by interpolating the created components of a synthetic sample using eqs. (4) and (5). The number of the obtained components at each grid point, which are called bootstrap samples, is equal to n_1 , since each component is interpolated from a single synthetic sample.

(5) A frequency distribution is drawn from the bootstrap samples at each position and the mean value μ_{kij} and the error range σ_{kij} are calculated for the velocity component u_{kij} .

Accordingly, the smoothed result $u_{ave,kij}^{n+1}$ is required to be contained within the following band width:

$$\begin{aligned} u_{\min,kij} &= \mu_{kij} - \sigma_{kij} \leq u_{ave,kij}^{n+1} \\ &\leq \mu_{kij} + \sigma_{kij} = u_{\max,kij}. \end{aligned} \quad (8)$$

The component u_{kij}^{n+1} is set at $u_{ave,kij}^{n+1}$ in case that eq. (8) is satisfied, otherwise u_{kij}^{n+1} is replaced by the minimum or maximum value of the band width. Thus

$$u_{kij}^{n+1} = \max\{u_{\min,kij}, \min(u_{\max,kij}, u_{ave,kij}^{n+1})\}. \quad (9)$$

The error range σ_{kij} is determined on the basis of a confidence level of 68%, which means 68% of the bootstrap samples are included in this range [19].

3.2. Calculation of vorticity

The vorticity vector ω in a three-dimensional flow is generally defined as

$$\begin{aligned} \omega &= \nabla \times \mathbf{u} = \left(\frac{\partial u_3}{\partial x_2} - \frac{\partial u_2}{\partial x_3} \right) \mathbf{i}_1 + \left(\frac{\partial u_1}{\partial x_3} - \frac{\partial u_3}{\partial x_1} \right) \mathbf{i}_2 \\ &\quad + \left(\frac{\partial u_2}{\partial x_1} - \frac{\partial u_1}{\partial x_2} \right) \mathbf{i}_3 \\ &= \omega_1 \mathbf{i}_1 + \omega_2 \mathbf{i}_2 + \omega_3 \mathbf{i}_3, \end{aligned} \quad (10)$$

where \mathbf{i}_1 , \mathbf{i}_2 and \mathbf{i}_3 are unit vectors in orthogonal coordinates. The third component ω_3 can be estimated from the two-dimensional velocity components interpolated on a uniform grid pattern by discretizing the corresponding term in eq. (10) as done by finite-difference techniques:

$$\omega_{3ij} = \frac{u_{2i+1,j} - u_{2i-1,j}}{2 \Delta x} - \frac{u_{1i,j+1} - u_{1i,j-1}}{2 \Delta x}, \quad (11)$$

where ω_{3ij} means the vorticity component at the grid point P_{ij} .

3.3. Estimation of uncertainty

Several investigations have been made to specify the sources of errors arising in a particle-tracking method and to evaluate their quantities [8–12]. As a result it can be seen that a large amount of the uncertainties involved in this method have been clarified so far. According to Agui and Jimenez [12], two different errors, the visualization error and the sampling error, need to be taken into account in this study.

The main sources associated with the visualization error are

- (1) positioning of tracer particles, and
- (2) traceability of the particles in the fluid.

The error of the particle positioning ϵ_η may be related to a large-scale resolution and a micro-scale one; the former resolution is derived from the relationship between the length of large-scale flow area, such as the depth of the hot plenum and the number of the pixels along its image. On the other hand, the micro-scale resolution is based on the scale of a particle and the number of the pixels of its image. Regarding the uncertainty of velocity vectors, the latter one is essential and designating its precision η , the relative error is estimated with respect to the representative velocity U_0 as

$$\epsilon_\eta = (\eta/\Delta)U_0 = 9.6 \times 10^{-2}U_0, \quad (12)$$

where Δ is the average length of particle trajectories. The average values of Δ and η are 1.2 mm and 0.12 mm, respectively.

The error ϵ_f arising from the traceability of the particles was investigated by Agui and Jimenez on the basis of Hinze's turbulence theory [20]. The error is evaluated as

$$\epsilon_f^2 = 1.8 \times 10^{-2} \frac{\gamma^2}{S_0^2} U_0^2, \quad (13)$$

where $\gamma = (\rho_p - \rho_f)/\rho_f$ and S_0 is Stokes number defined as $S_0 = (\nu/\omega_0)^{1/2}/D$, where D and ω_0 are the diameter of the particle, which is 0.4 mm in our experiments, and the lowest turnover frequency of the large eddies, respectively. Assuming that ω_0 is calculated from U_0 and L_0 in table 2, the approximate value of S_0 equals 20. Since saline water was used as a working fluid to minimize γ in our experiments, γ is expected to be nearly zero. Nevertheless, if assuming the worst situation in which the fluid is pure water, the largest error ϵ_f conceivable is estimated as

$$\epsilon_f = 2.0 \times 10^{-4}U_0. \quad (14)$$

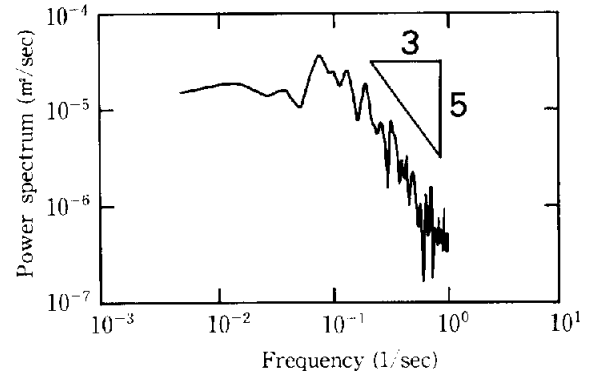


Fig. 5. Example of power spectrum for fluctuating velocity.

Since the two errors, ϵ_η and ϵ_f , are independent, the visualization error ϵ_{vis} is calculated by

$$\epsilon_{vis}^2 = \epsilon_\eta^2 + \epsilon_f^2 = 9.6 \times 10^{-2}U_0^2. \quad (15)$$

The sampling error ϵ_{sam} , which results from the amplitude of the velocity fluctuation, is indicated by the following equation [12], when the power spectrum of the velocity fluctuations behaves as λ^n :

$$\epsilon_{sam} = u' \left(\frac{3\eta U_0}{Lu'} \right)^{(n-1)/(n+1)}, \quad (16)$$

where λ is the wavelength, u' is the fluctuating velocity and L stands for the large scale of the flow, which may correspond to the length scale L_0 in table 2. Representative values for n and u'/U_0 can be estimated by turbulence measurements using a laser-Doppler velocimetry system. Figure 5 presents an example of the power spectrum observed near the core outlet, which gives $n = 5/3$. While the ratio u'/U_0 depends on the location within the flow, it is roughly of the order one on the basis of the turbulence measurements. As a result, the sampling error is estimated as

$$\epsilon_{sam} = 0.16U_0. \quad (17)$$

Assuming the two errors, ϵ_{vis} and ϵ_{sam} , are independent, the total error with respect to the velocity is estimated as

$$\epsilon^2 = \epsilon_{vis}^2 + \epsilon_{sam}^2 = 3.6 \times 10^{-2}U_0^2. \quad (18)$$

From the above estimation, it can be seen that the error ranges belonging to our image processing method are acceptable.

4. Experimental results

The visualized particles were continuously recorded on video tapes from the initial condition in all experimental cases shown in table 1. Along with this video recording, the temperature distributions around the heater were monitored by thermistors to examine the transition from the initial situation to the steady state. As a result, it was observed that in general the steady state was attained at approximately $t^* = 10$, where t^* is the time after the start of the experiment normalized with respect to the representative time t_0 in table 2. Taking account of this, the video images were analyzed at around $t^* = 0.4, 1.5, 4.0$ and 25.0 , of which the former three are in the transient situation and the last one in the steady state.

At each time, velocity vectors from 10 frames were obtained during 45-second periods, which is sufficiently shorter than t_0 . Thus the vector distribution averaged over 10 frames can be interpreted as instantaneous results rather than long-time averages. About 4000 raw vectors were obtained from 10 frames and they were

eventually interpolated to nearly 2000 vectors, yet, for convenience, just a quarter of the interpolated vectors are presented in the final results. Thus the interval of the vectors presented in figs. 6 to 8 equals approximately 26 mm ($= 2\Delta x_1 = 2\Delta x_2$). These figures also present the vorticities, in which the contour lines for positive and negative values are drawn by solid and broken lines, respectively.

In Case-A35 presented in fig. 6, the main flow crosses diagonally from the inlet of the hot plenum to the IHX window at $t^* = 0.45$. The crossing flow is accompanied on both sides by some eddies, whose vorticities show opposite signs. As the time t^* increases, thermal stratification develops from the lower region of the plenum with increases in the temperature gradient and there appear several layers consisting of horizontal flows moving alternately in opposite directions. It was also observed that, since the actual eddies arising in the plenum are three-dimensional and their cross sections on the vertical plane are identified here, continuity of the fluid appears not to be satisfied on the vector maps. A similar tendency is also seen in

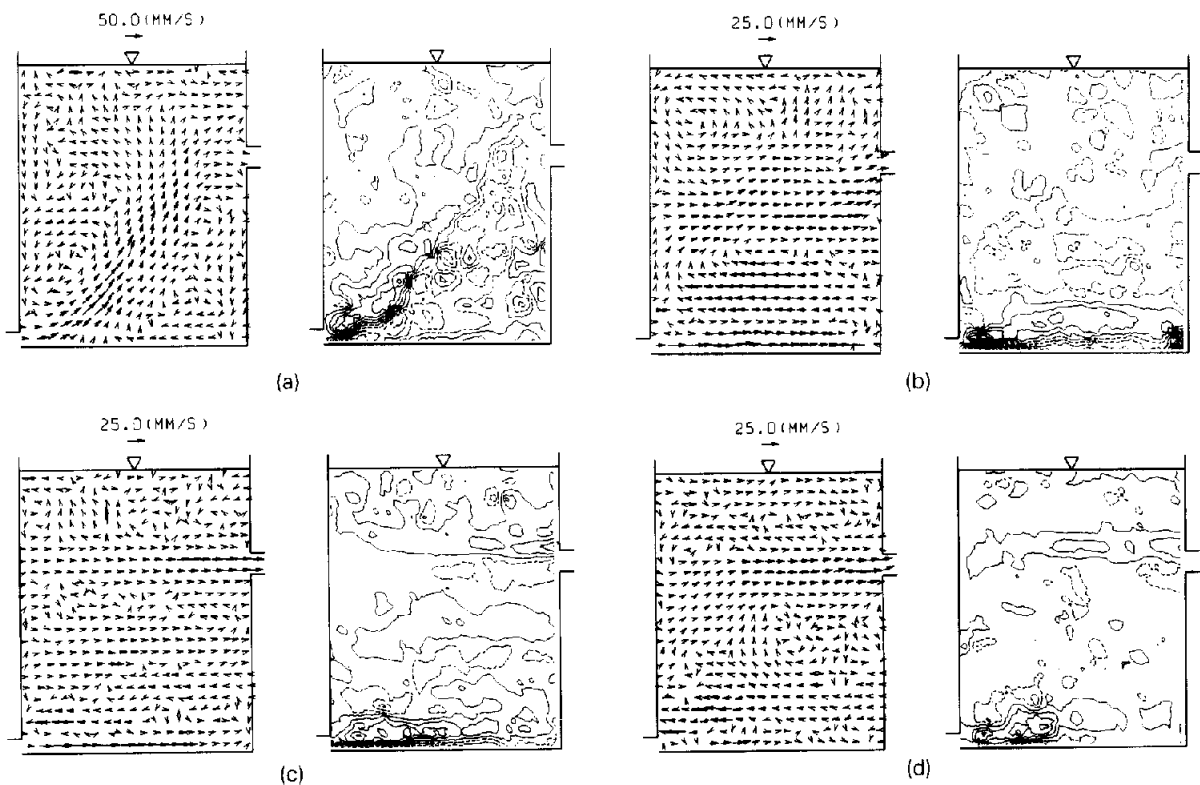


Fig. 6. Velocity vectors and vorticities measured in Case-A35; (a) $t^* = 0.45$, (b) $t^* = 1.59$, (c) $t^* = 4.53$, (d) $t^* = 27.17$.

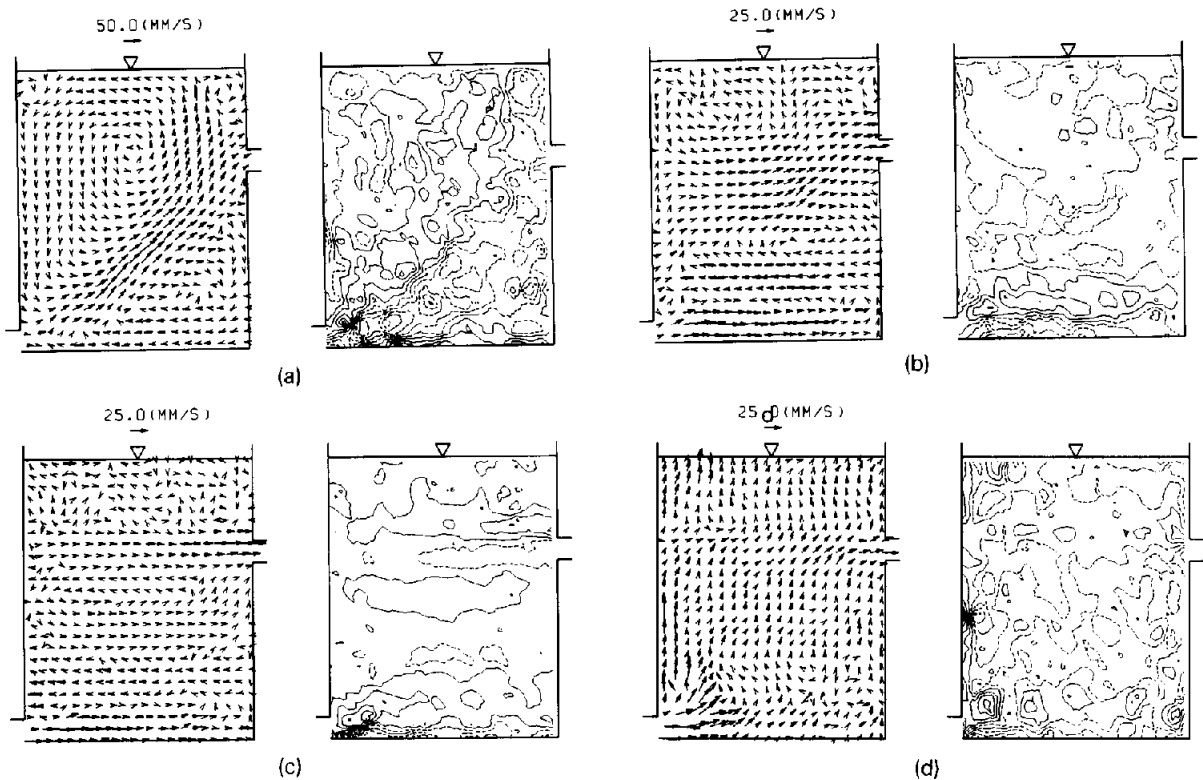


Fig. 7. Velocity vectors and vorticities measured in Case-A50; (a) $t^* = 0.31$, (b) $t^* = 1.10$, (c) $t^* = 3.13$, (d) $t^* = 18.80$.

Case-A50 presented in fig. 7, yet the flow pattern under steady state is largely different from that of Case-A35. The incoming flow is separated into horizontal and vertical ones near the inlet, probably because of the wider clearance near the inlet. The vertical flow runs up along the ACS side surface, while the horizontal flow is not dominant and changes itself into weak vertical movements in a short distance, leaving the right corner on the bottom stagnant. Figure 8 presents the results in Case-B35, in which the initial temperature was set lower than in the two previous cases. The diagonally crossing flow is also observed at $t^* = 0.55$ in this case. However, the flow pattern changes drastically at $t^* = 1.94$ and a vertical flow is formed along the ACS side wall, due to a higher temperature in the flow than in the ambient water of the hot plenum. As the mixing process proceeds, the dominant flow pattern disappears in the plenum and the flow comes to consist of many unsteady eddies.

5. Conclusion

An image processing system based on a particle-tracking method has been developed giving emphasis to automatic digitization, interpolation and smoothing techniques, and estimation of measurement uncertainties. The visualized movements of particles scattered in a fluid are recorded on video tapes and then converted to digital data automatically by an image processor. The acquisition of velocity vectors, their interpolation and other numerical analyses are performed on a computer. Our image processing system was applied to the natural convection flow in a simple 1/10 scale reactor model. As a result, the velocity vectors and the vorticities on a vertical cross section were measured under transient and steady states for different experimental cases. While it may not be easy to predict natural convection flows in the FBR hot plenum directly from the results obtained in our basic experiments, it can be

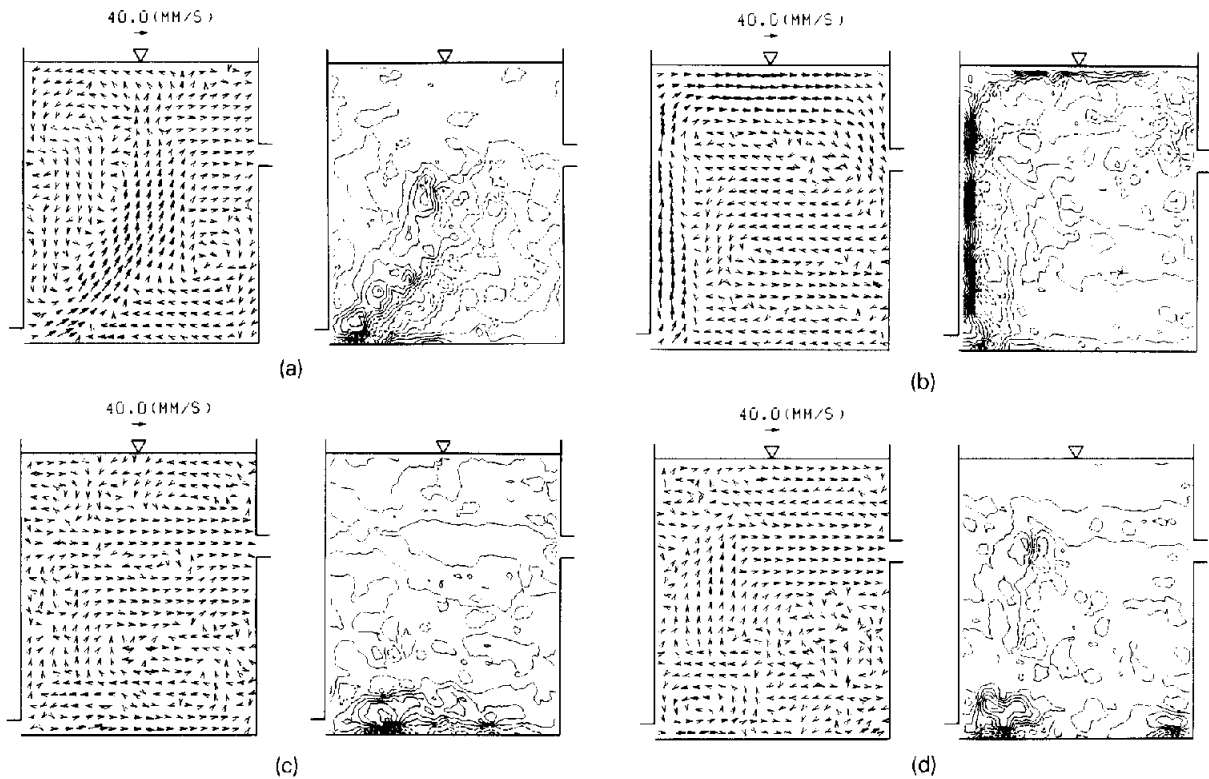


Fig. 8. Velocity vectors and vorticities measured in Case-B35; (a) $t^* = 0.55$, (b) $t^* = 1.94$, (c) $t^* = 5.53$, (d) $t^* = 33.18$.

seen that the geometry of the structures and the initial temperature distributions largely influence the aspects of natural convection flows. It is expected that our image processing method can play an important role to determine the quantitative flow behavior in experiments using water as a simulant fluid.

Acknowledgement

The authors would like to thank Dr. Y. Miyanaga for designing and constructing the experimental tank. Thanks are also due to Mr. J. Kanno for his substantial contribution to this work.

Nomenclature

D diameter of a particle,
 g gravity,
 H height of the above core structure.

H_w window width for interpolation; see eq. (5),
 i_k unit vectors in the direction of x_k ; $k = 1, 2, 3$,
 L length scale of a flow,
 L_0 representative macro-length scale,
 n_1 number of synthetic samples,
 N average number of particles per unit surface,
 N_1 number of velocity components in a base sample,
 P_0 output of the heater,
 Pe Péclet number; see eq. (3),
 P_{ij} regular grid point,
 P_m particle position,
 Q_s flow rate of secondary loop,
 Re Reynolds number; see eq. (2),
 Ri Richardson number; see eq. (1),
 S_0 Stokes number; $S_0 = (\nu/\omega_0)^{1/2}/D$,
 t time; $t = 0$ corresponds to the time at initial conditions,
 t^* non-dimensional time; $t^* = t/t_0$,

t_0	representative time,
T_0	initial temperature in the hot plenum,
T_s	temperature of secondary loop,
\mathbf{u}	velocity vector,
u'	fluctuating velocity,
$u_{ave,n+1}^{n+1}$	average velocity component at step $n+1$; see eq. (7),
u_k	horizontal ($k=1$), vertical ($k=2$) and transverse ($k=3$) velocity components,
u_{kij}	velocity components at P_{ij} ; $k=1, 2$,
u_{kij}^n	smoothed velocity components at step n ; see eq. (9),
u_{km}	velocity components at P_m ; $k=1, 2$,
$u_{max,kij}$	maximum velocity components of the band width; see eq. (8),
$u_{min,kij}$	minimum velocity components of the band width; see eq. (8),
U_0	representative velocity,
x_k	horizontal ($k=1$), vertical ($k=2$) and transverse ($k=3$) coordinates,
x_{kij}	location at P_{ij} ; $k=1, 2$,
x_{km}	location at P_m ; $k=1, 2$.

Greek symbols

α	thermal diffusivity,
α_m	weighting coefficient; see eq. (5),
β	thermal expansion coefficient,
γ	non-dimensional particle density in a fluid; $\gamma = (\rho_p - \rho_f) / \rho_f$,
δ	mean distance between particles,
Δ	average length of particle trajectories,
Δl	distance between initial and terminal center points,
Δt	time interval to obtain trace image,
ΔT	maximum temperature difference in the ex- perimental tank,
$\Delta x_1, \Delta x_2$	horizontal and vertical intervals on regular grids; $\Delta x_1 = \Delta x_2$,
ϵ	total error,
ϵ_f	traceability error; see eq. (16),
ϵ_{sam}	sampling error; see eq. (15),
ϵ_{vis}	visualization error; see eq. (12),
ϵ_η	particle positioning error,
η	precision on particle positioning,
λ	wavelength,
μ_{kij}	mean value of bootstrap samples for u_{kij} ,
μ_{km}	mean value of bootstrap samples for u_{km} ,
ν	kinematic viscosity,
ρ_f	fluid density,
ρ_p	particle density,
σ_{kij}	error range of bootstrap samples for u_{kij} ,

σ_{km}	standard deviation of bootstrap samples for u_{km} ,
ω	vorticity vector; see eq. (10),
ω_0	the lowest turnover frequency,
$\omega_1, \omega_2, \omega_3$	components of vorticity vector; see eq. (10),
ω_{3ij}	ω_3 at P_{ij} ; see eq. (11).

References

- [1] D. Weinberg, D. Suckow, U. Muller and H. Hoffmann, The transferability to reactor conditions of thermohydraulics model investigations of decay heat removal, ANS Int. FRS Meeting, Snowbird, Utah, 1990.
- [2] J.J. Oras, T.M. Kuzay and K.E. Kasza, Overview of the ANL advanced LMR system thermal-hydraulics test program supporting both GE/PRISM and RI/SAFER, Proc. 3rd Int. Symp. RFMTM, Tokyo, 1988, pp. 435–445.
- [3] H. Hoffmann, D. Weinberg and Y. Ieda, Thermohydraulic investigations of decay heat removal systems by natural convection for liquid-metal fast breeder reactors, Nucl. Technol. 88 (1989) 75–86.
- [4] M. Akustu, Y. Okabe, K. Satoh, H. Kamide, K. Hayashi, N. Naohara, K. Iwashige and Y. Shibata, Study of thermal hydraulic characteristic during decay heat removal for pool type FBR, Nucl. Technol., to be published.
- [5] L. Hesselink, Digital image processing in flow visualization, Annu. Rev. Fluid Mech. 20 (1988) 421–485.
- [6] E.F.C. Sommerscales, Fluid velocity measurements by particle tracking, in: R.E. Wendt, ed., Its Measurement and Control in Science and Industry, Vol. I (Instrum. Soc. Am., 1980) pp. 795–808.
- [7] L. Prandtl and O. Tietjens, Applied Hydro and Aerodynamics (Dover, New York, 1934).
- [8] K. Imaichi and K. Ohmi, Numerical processing of flow-visualization pictures – measurement of two-dimensional vortex flow, J. Fluid Mech. 129 (1983) 283–311.
- [9] K. Nishino, N. Kasagi and M. Hirata, Three-dimensional particle tracking velocimetry based on automated digital image processing, J. Fluids Engrg. 111 (1989) 384–391.
- [10] T. Kobayashi, Y. Yoshitake, T. Saga and S. Segawa, An image processing technique for determining two-dimensional flow fields with reverse flow, Proc. ASME Symp. on Physical and Numerical Flow Visualization, 1985, pp. 39–46.
- [11] T.P.K. Chang, A.T. Watson and G.B. Tatterson, Image processing of tracer particle motions as applied to mixing and turbulent flow – II. Results and discussion, Chem. Engrg. Sci. 40 (2) (1985) 277–285.
- [12] J. Agui and J. Jimenez, On the performance of particle tracking, J. Fluid Mech. 185 (1987) 447–468.
- [13] T. Utami and T. Ueno, Visualization and picture processing of turbulent flows, Exp. Fluids 2 (1984) 25–32.
- [14] K.A. Marko and L. Rimai, Video recording and quantitative analysis of seed particle track images in unsteady flows, Appl. Opt. 24 (21) (1985) 3666–3672.

- [15] R.G. Racca and J.M. Dewey, A method for automatic particle tracing in a three-dimensional flow field, *Experiments in Fluids* 6 (1988) 25–32.
- [16] L.J. Chen, J.A. Walter and C.J. Chen, Qualitative and quantitative flow visualization of flow past a cubic chamber with offset inlet and outlet, 4th Int. Symp. on Refined Flow Modelling and Turbulence Measurements, 1990, pp. 538–545.
- [17] B. Efron, Computers and the theory of statistics: thinking the unthinkable, *SIAM Rev.* 21 (4) (Oct. 1979) 460–480.
- [18] B. Efron, Estimating the error rate of a prediction rule: improvement of cross-validation, *J. Am. Stat. Assoc.* 78 (382) (June, 1983) 316–331.
- [19] P. Diaconis and B. Efron, Computer-intensive methods in statistics, *Sci. Am.* 248 (5) (1983) 96–109.
- [20] J.O. Hinze, *Turbulence* (McGraw-Hill, New York, 1959).